OBLIQUITY CORRECTION FOR REVERSE TIME MIGRATION

F. A. Silva Neto, J. C. Costa, M. Rian, J. Schleicher, and A. Novais

email: *js@ime.unicamp.br*

keywords: *Reverse time migration, imaging condition, illumination compensation, true amplitude*

ABSTRACT

The quality of seismic images obtained by reverse time migration strongly depend on the employed image condition. We propose a new imaging condition, which is motivated by stationary phase analysis of the classical cross-correlation imaging condition. Its implementation requires the Poynting vector of the source and receiver wavefields at the imaging point. An obliquity correction is added to compensate for the reflector dip effect on amplitudes of reverse time migration. Numerical experiments show that using an imaging condition with obliquity compensation improves reverse time migration by reducing backscattering artifacts and improving the illumination compensation.

INTRODUCTION

Pre-stack reverse time migration (RTM) is based on the time reversal property of the two-way wave equation and the cross-correlation imaging condition proposed by Claerbout (1985). Several implementations of RTM using this imaging condition have been reported (McMechan, 1983; Kosloff and Baysal, 1983; Baysal et al., 1983).

The computational demand for RTM is high compared to wave equation migration by downward extrapolation of the wavefield (Biondi, 2006). However, low cost parallel computing and more efficient storage hardware is making RTM feasible. The difficulties of seismic imaging below the salt column and in areas of high lateral velocity variation have drawn attention to RTM, which, at least theoretically, is able to meet those challenges.

RTM has its limitations, though. Two major drawbacks are the artifacts produced by backscattering and the amplitudes of the migrated images, which are not proportional to the subsurface reflectivity (Biondi, 2006). To reduce the artifacts due to backscattering, several approaches have been recently proposed. Guitton et al. (2007) use a least-squares regularization; Fletcher et al. (2005) introduced a new forward wave-equation to attenuate backscattering events and Yoon and Marfurt (2006) introduced the Poynting vector imaging condition.

Several attempts to improve the amplitudes in RTM are based on illumination compensation with different kinds of regularization (Valenciano and Biondi, 2003; Kaelin and Guitton, 2006). Attempting to better understand the amplitudes in RTM, Matthew et al. (2005) performed an asymptotic analysis of the cross-correlation imaging condition. Their analysis assumes a single planar reflector in a 3D homogeneous medium, full coverage, and infinite aperture. They demonstrate that the amplitudes of RTM are affected by an obliquity factor that depends on the reflector dip. Based on this result, we propose an imaging condition which can asymptotically correct for this obliquity factor in RTM. We present numerical experiments that show the improvement of RTM images when the obliquity and illumination compensation are applied in the imaging condition. Numerical experiments demonstrate the improvement of the images when the obliquity factor and illumination compensation are included in the imaging condition for RTM.

METHOD

We start revisiting the asymptotic analysis of the cross-correlation imaging condition (Matthew et al., 2005). Based on this result we propose an imaging condition for RTM which, asymptotically, improves the amplitude of RTM images.

Asymptotic analysis of cross-correlation imaging condition

The cross-correlation imaging condition for shot-profile migration (Claerbout, 1985)

$$I(\mathbf{x}) = \sum_{\mathbf{x}_s} \sum_{\mathbf{x}_r} \int_0^{t_{max}} p_s(\mathbf{x}, t; \mathbf{x}_s)\, p_r(\mathbf{x}, t; \mathbf{x}_r) dt, \tag{1}$$

produces an image, $I(\mathbf{x})$, through the cross-correlation, with zero lag, of two wavefields; $p_s(\mathbf{x}, t; \mathbf{x}_s)$ represents the forward propagated wavefield from the source, $\mathbf{x}_s$, to the imaging point, $\mathbf{x}$; $p_r(\mathbf{x}, t; \mathbf{x}_r)$ represents the receiver wavefield that is backpropagated in reverse time from the receiver, $\mathbf{x}_r$, to the imaging point. Moreover, t_{max} is maximum recorded time.

The asymptotic analysis of imaging condition (1) was presented by Matthew et al. (2005). They assumed a single planar reflector, with dip angle D along the x coordinate direction; a homogeneous medium with P velocity c_P, and unlimited coverage of sources and receivers. We use the method of stationary phase and re-derive the high frequency approximation for (1). Our result (see Appendix I) is

$$I(\mathbf{x}) \approx \pi C^3 c_P^3 \frac{R(\mathbf{x}_0, \mathbf{x}_0)}{\cos^3 D} \frac{1}{\xi} w'' \left(\frac{2 \cos D}{c_P} \xi \right) \otimes w'' \left(\frac{2 \cos D}{c_P} \xi \right) , \tag{2}$$

where $\xi = z - z_R$, with z_R being the depth of the reflector at the horizontal position (x, y) of the image point $\mathbf{x} = (x, y, z)$. Also, $R(\mathbf{x}_0, \mathbf{x}_0)$ is the normal incidence reflection coefficient, C is a constant, and $w(t)$ is the source pulse. Moreover, symbol $\otimes$ stands for the convolution operation.

Expression (2) differs from the result of Matthew et al. (2005) only by the presence of the pulse-stretch factor, $2 \cos D / c_P$ in the arguments of both the wavelets. As pointed out by Matthew et al. (2005), for this simple example, we note that (a) the geometrical spreading is corrected even with no amplitude compensation term in the imaging condition; (b) the pulse is antisymmetric relative to the reflector position; (c) the pulse amplitude decays with the distance from the reflector; (d) the obliquity factor $1/\cos^3 D$, increases the amplitude with the reflector dip as in Kirchhoff migration. In the next section we propose an imaging condition that can compensate for this amplitude distortion.

Obliquity factor compensation

The Poynting-vector imaging condition proposed by Yoon and Marfurt (2006), without the illumination compensation,

$$I(\mathbf{x}) = \int_{\mathbf{x}_s} \int_{\mathbf{x}_r} \int_0^{t_{max}} W(\mathbf{S}_s, \mathbf{S}_r) p_s(\mathbf{x}, t; \mathbf{x}_s)\, p_r(\mathbf{x}, t; \mathbf{x}_r) dt d\mathbf{x}_s d\mathbf{x}_r \ , \tag{3}$$

adds a weight $W(\mathbf{S}_s, \mathbf{S}_r)$ to operation (1); in this expression, the Poynting vector $\mathbf{S}$ represents the acoustic power flux, given by

$$\mathbf{S} = p\mathbf{v} \ , \tag{4}$$

where p represents pressure and $\mathbf{v}$ particle velocity. The subscripts s and r indicate the power flux associated to the source and receiver wavefields. The weight function $W(\mathbf{S}_s, \mathbf{S}_r)$ was proposed to filter events considered for imaging based on the scattering angle, γ. Yoon and Marfurt (2006) proposed to use

$$\cos \gamma = \frac{\mathbf{S}_s \cdot \mathbf{S}_r}{\|\mathbf{S}_s\| \|\mathbf{S}_r\|} \tag{5}$$

to set a maximum scattering angle for the events used for image forming, i.e., the weight $W(\mathbf{S}_s, \mathbf{S}_r)$ is calculated as

$$W(\mathbf{S}_s, \mathbf{S}_r) = \begin{cases} 1 & \text{if } \gamma < \gamma_{\max}, \\ 0 & \text{otherwise.} \end{cases} \tag{6}$$

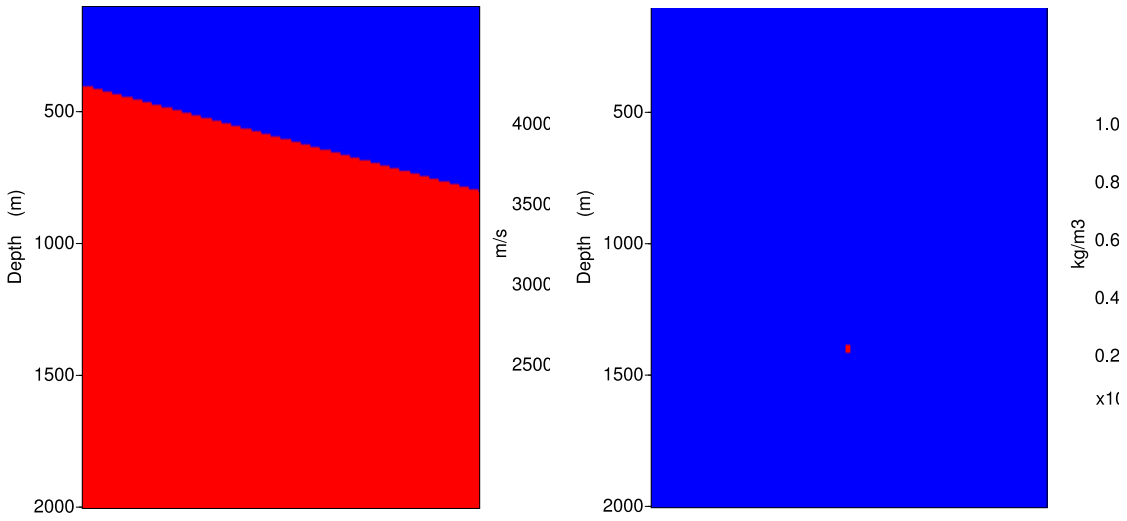

(a) (b)

Figure 1: (a) Velocity model; (b) Density model.

A disadvantage of this weight is its dependence on the choice of the maximum angle $\gamma_{\max}$, for which no obvious physical criteria are available.

We propose to use the Poynting vector information to compensate for the obliquity factor in (2). The bisection angle, $\alpha = \gamma/2$, can be detected from

$$\cos^2 \alpha = \frac{1}{2}\left(1 + \frac{\mathbf{S}_s \cdot \mathbf{S}_r}{\|\mathbf{S}_s\|\|\mathbf{S}_r\|}\right) . \tag{7}$$

It will give the reflector dip for a reflection event. For this simple model, taking $W(\mathbf{S}_s, \mathbf{S}_r) = \cos^3 \alpha$ in equation (3), and applying the same stationary phase analysis described above, we arrive at (2) without the obliquity factor. For the 2D case, the obliquity compensation is achieved with $W(\mathbf{S}_s, \mathbf{S}_r) = \cos^{5/2} \alpha$.

The analysis above is simple and does not take into account other issues that affect amplitude when applying RTM in complex velocity models, like the lack of full coverage of sources and receivers and the uneven illumination of the targets. Illumination compensation is achieved normalizing the cross-correlation imaging condition by the source energy at the imaging point (Biondi, 2006). We propose to combine the obliquity factor weight and illumination compensation in the imaging condition

$$I(\mathbf{x}) = \int_{\mathbf{x}_s}\int_{\mathbf{x}_r} \frac{\int_0^{t_{max}} W(\mathbf{S}_s, \mathbf{S}_r) p_s(\mathbf{x}, t; \mathbf{x}_s)\, p_r(\mathbf{x}, t; \mathbf{x}_r) dt}{\int_0^{t_{max}} p_s(\mathbf{x}, t; \mathbf{x}_s)\, p_s(\mathbf{x}, t; \mathbf{x}_s) dt} d\mathbf{x}_s d\mathbf{x}_r \ . \tag{8}$$

This imaging condition will be evaluated in the next section by means of numerical experiments.

NUMERICAL EXAMPLES

We evaluate the imaging condition with obliquity compensation on two synthetic data sets. In each experiment, we applied RTM using four types of imaging conditions: cross-correlation, cross-correlation with illumination compensation, Poynting vector with illumination, and the proposed imaging condition (8). We did not apply any regularization strategy to the denominator of the imaging conditions with illumination compensation. In all experiments we used $\gamma_{\max} = 120°$, i.e., $\cos\gamma > -1/2$, as the cutoff for the Poynting-vector imaging condition. The first numerical example images a single shot in a medium with a planar reflector and a point diffractor. We used the velocity and density model presented in Figure 1 to compute the synthetic data in Figure 2. The minimum offset is 140 m and the maximum offset 1500 m, receiver

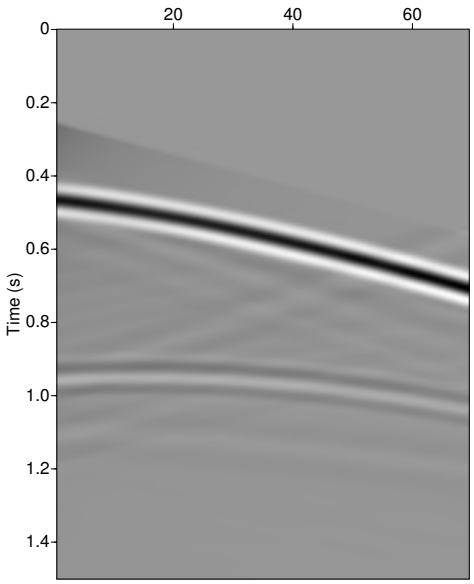

Figure 2: Single shot data after muting the direct arrival.

spacing is 20 m. Figure 3 shows the results of RTM using standard cross-correlation and cross-correlation with illumination compensation. Figure 4 shows the results of RTM using the Poynting-vector imaging condition with illumination compensation and using the proposed imaging condition. We notice the strong artifact near the source in Figure 3a and the week amplitude at the diffractor. Figure 3b shows the diffractor with stronger amplitude and the reduction of artifacts near the source. The Poynting vector imaging condition (Figure 4a) produced about the same results as in Figure 3b. The proposed imaging condition presents reduced artifacts near the source when compared to the previous imaging conditions.

The second numerical example presents RTM results for the Marmousi data set (Versteeg and Grau, 1990). The data set has 240 shots, each common shot gather has 96 receivers and 200 m minimum offset; the distance between shots is 25 m, which is the same distance between receivers. The original Marmousi velocity model is depicted in Figure 5a. A smoothed version of this model (Figure 5b) was used for RTM in order to reduce backscattering. The RTM images using cross-correlation imaging condition, with and without illumination compensations are presented in Figure 6. The dark artifacts in the upper left part of these figures and the white spots in the bottom right of these figures are caused by backscattering. The artifacts are much reduced using the Poynting vector image condition (Figure 7a), though some artifacts still remain in the upper left part of the image. The image produced with obliquity compensation (Figure 7b) presents fewer artifacts than the all the previous imaging conditions. It also has improved amplitudes at the bottom around the reservoir region. More investigation is required in order to combine obliquity compensation with regularized illumination compensation (Valenciano and Biondi, 2003). However, our numerical experiments indicate that obliquity compensation can improve RTM images.

CONCLUSIONS

We proposed and evaluated a new imaging condition for reverse time migration. This imaging condition was motivated by a stationary phase analysis of the cross-correlation imaging condition in a homogeneous medium with a single planar reflector and illumination compensation. The new imaging condition incorporates a dip-dependent weight function. Its implementation requires Poynting-vector information of the source and receiver wavefields at the imaging point. Numerical experiments using the Marmousi data support our claim that the proposed imaging condition reduces backscattering artifacts in RTM. These results are even more interesting considering that no regularization strategy was applied to the imaging conditions under consideration.

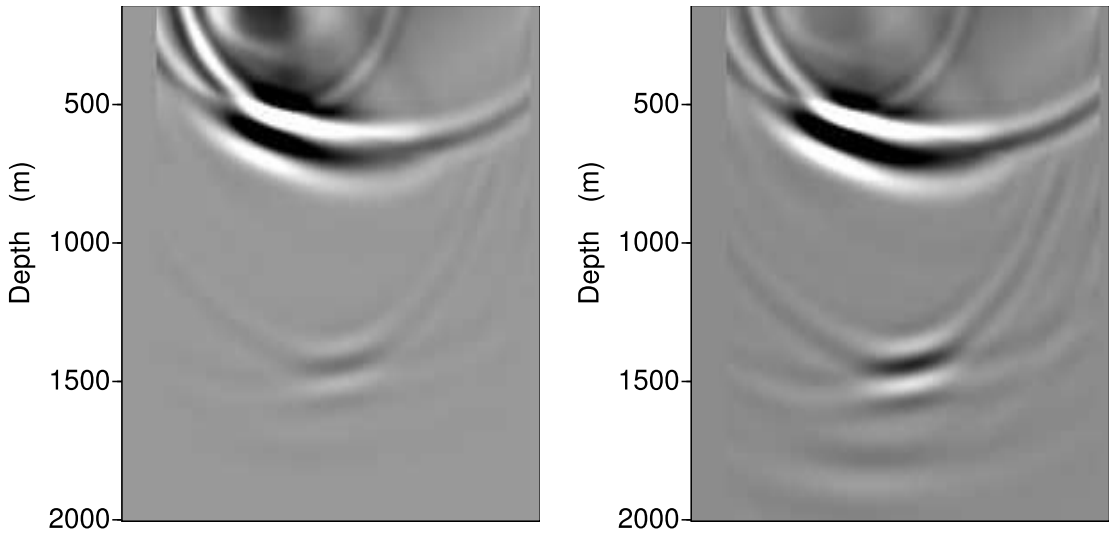

(a) (b)

Figure 3: Imaging condition: (a) cross-correlation; (b) cross-correlation with illumination compensation.

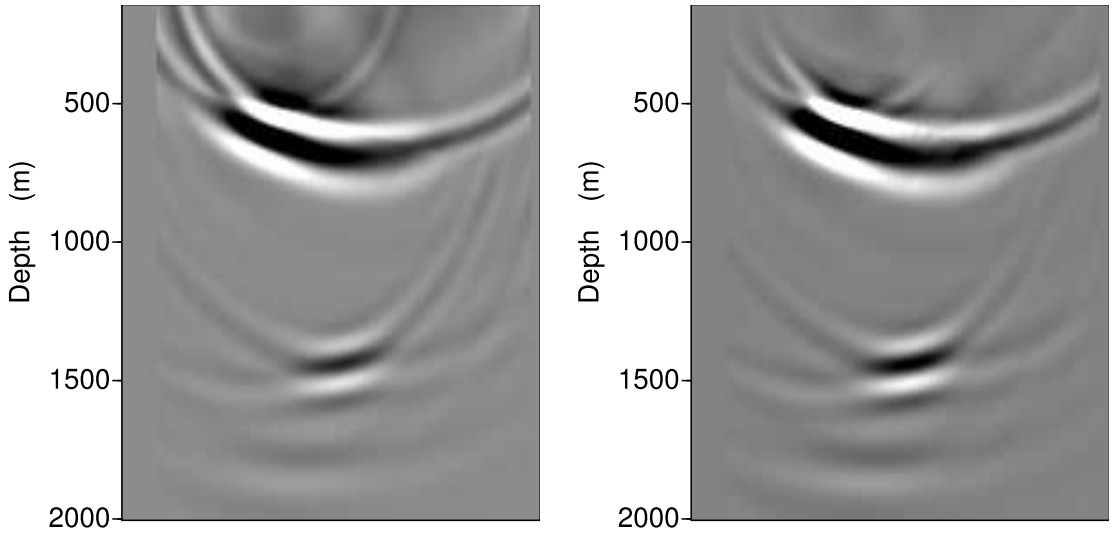

(a) (b)

Figure 4: Imaging condition: (a) Poynting vector; (b) obliquity correction plus illumination compensation.

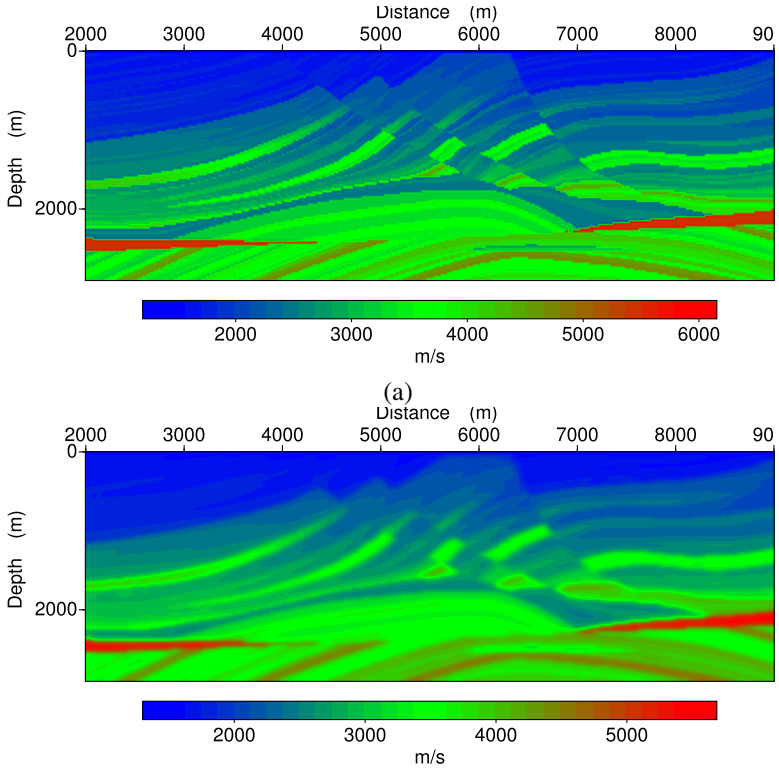

Figure 5: (a) Marmousi model; (b) Smoothed RTM velocity model.

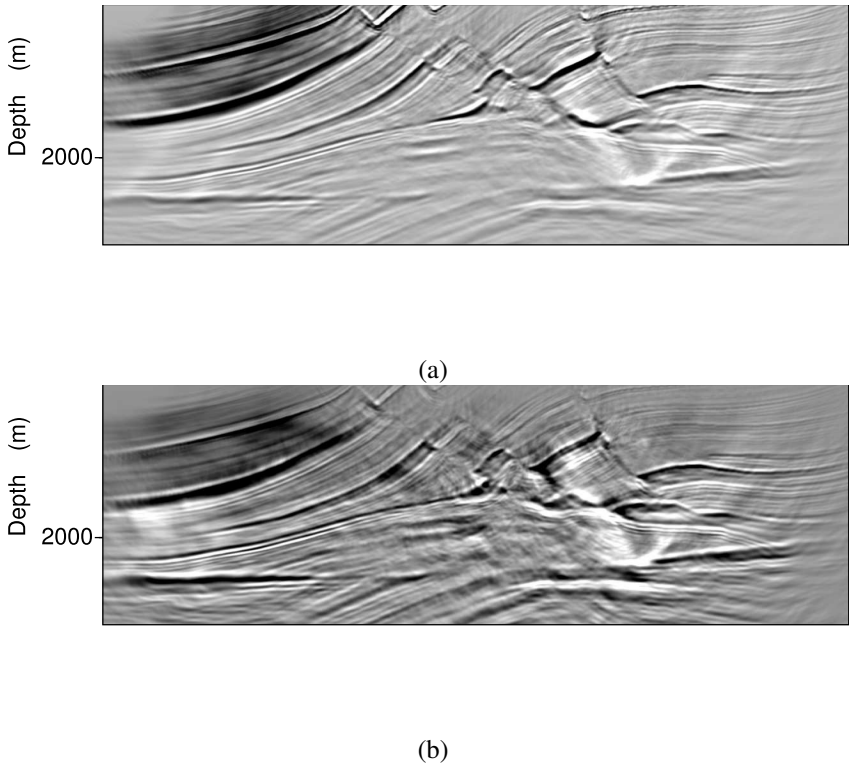

Figure 6: Imaging condition: (a) cross-correlation; (b) cross-correlation plus illumination compensation.

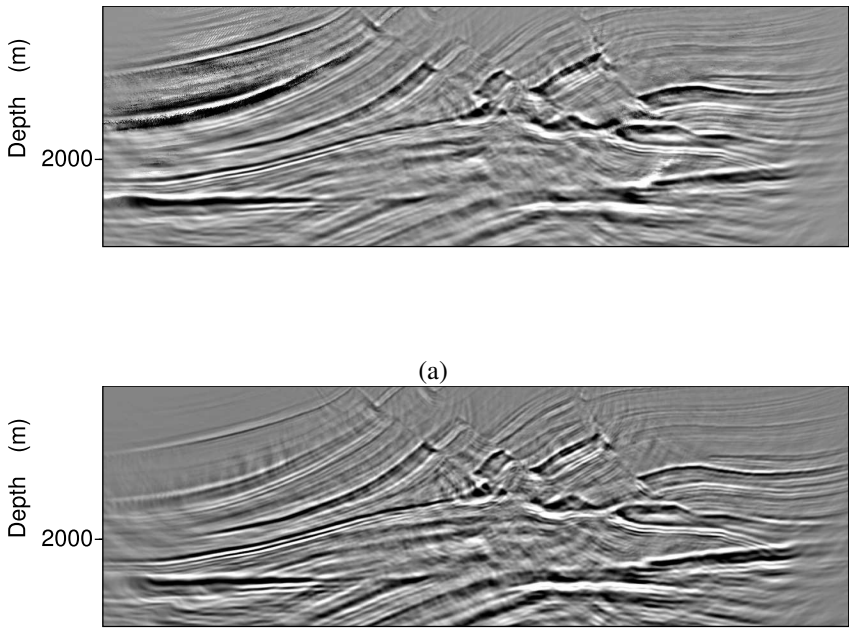

Figure 7: Imaging condition: (a) Poynting vector; (b) obliquity correction plus illumination compensation.

ACKNOWLEDGMENTS

This research was supported in part by CNPq, FAPESP, and the sponsors of the WIT consortium. Maiton Rian also thanks the SBGf for financial support.

REFERENCES

Baysal, E., Kosloff, D., and Sherwood, W. (1983). Reverse time migration. *Geophysics*, 11(48):1514–1524.

Biondi, B. (2006). *3D seismic imaging*. Society of Exploration Geophysicists.

Bleistein, N. and Handelson, R. A. (1975). *Asymptotic expansions of integrals*. Dover.

Bracewell, R. (1999). *The Fourier Transforms and Its applications*. McGraw-Hill Science.

Cerveny, V. (2001). *Seismic ray theory*. Cambridge University Press.

Claerbout, J. (1985). *Imaging the earth's interior*. Blackwell Scientific Publications.

Fletcher, R. F., Fowler, P., Kitchenside, P., and Albertin, U. (2005). Suppressing artifacts in prestack reverse time migration. *SEG International Annual Meeting*, 24:2049–2051.

Guitton, A., Kaelin, B., and Biondi, B. (2007). Least-squares attenuation of reverse-time-migration artifacts. *Geophysics*, pages S19–S23.

Kaelin, B. and Guitton, A. (2006). Imaging condition for reverse time migration. *SEG International Annual Meeting*, 25:2594–2597.

Kosloff, D. and Baysal, E. (1983). Migration with the full wave equation. *Geophysics*, 6(48):677–687.

Matthew, M. H., Bartel, L., Aldridge, D., and Symons, N. (2005). Insight into the output of reverse-time migration: what do amplitudes mean? *SEG International Annual Meeting*.

McMechan, G. A. (1983). Migration by extrapolation of time-dependent boundary values. *Geophysical Prospecting*, 31(3):413–420.

Valenciano, A. and Biondi, B. (2003). 2-D deconvolution imaging condition for shot-profile migration. *SEG International Annual Meeting*, 23:2431–2433.

Versteeg, R. and Grau, G. (1990). Pratical aspects of seismic data inversion, the Marmousi experience. *52nd EAEG Meeting. Eur. Assoc. Expl. Geophys., Proceedings of 1990 EAEG Workshop*, pages 1–194.

Yoon, K. and Marfurt, K. (2006). Reverse-time migration using the Poynting vector. *Exploration Geophysics*, 37:102–107.

APPENDIX A

STATIONARY-PHASE ANALYSIS OF REVERSE TIME MIGRATION

In this appendix, we asymptotically analyze reverse time migration following the lines of Matthew et al. (2005). Specifically, we apply the method of stationary phase (see, e.g., Bleistein and Handelson, 1975) to integral (1) for the situation of a planar dipping interface in a homogeneous medium and a set of common-shot records with unlimited acquisition aperture both in source and receiver coordinates. Our result differs from the one of Matthew et al. (2005) by a pulse-stretch factor that depends on the reflector dip.

Reflection from a dipping reflector

We start by considering a dipping reflector. Without loss of generality, we assume the x-axis to be oriented in the down-dip direction so that the dip angle D is the angle between the reflector and the x-axis. Then, a point on the reflector has the coordinates

$$\mathbf{x}_R(x,y) = x\,\mathbf{e}_1 + y\,\mathbf{e}_2 + (z_d + x\tan D)\,\mathbf{e}_3, \tag{9}$$

where $\mathbf{e}_i$ ($i = 1,2,3$) are the unit vectors in the coordinate directions and where z_d is the depth of the reflector at $x = y = 0$.

To describe the source wavefield $p_s(\mathbf{x},t;\mathbf{x}_s,0)$ at the image point, we consider the point source at $\mathbf{x}_s$ to be a volume injection source described by $q(\mathbf{x},t) = \delta(\mathbf{x}-\mathbf{x}_s)w(t)$. Here, $w(t)$ represents the source pulse and $\mathbf{x}_s = (x_s, y_s, 0)$ describes the coordinates of the source at the surface. Then, the pressure field produced by such a source is given by

$$p_s(\mathbf{x},t;\mathbf{x}_s,0) = \frac{C}{|\mathbf{x}-\mathbf{x}_s|}w'\left(t - \frac{|\mathbf{x}-\mathbf{x}_s|}{c_P}\right) \tag{10}$$

where the prime denotes the time derivative. Also, c_P is the wave velocity and C is a constant (Cerveny, 2001). For an acoustic medium with constant density ρ, we have $C = 1/4\pi\rho$. Correspondingly, the reflected pressure field registered by a geophone at $\mathbf{x}_g = (x_g, y_g, 0)$ can be expressed as

$$p_g(\mathbf{x}_g,t;\mathbf{x}_s,0) = \frac{CR(\mathbf{x}_g,\mathbf{x}_s)}{|\mathbf{x}_g-\mathbf{x}_s^I|}w'\left(t - \frac{|\mathbf{x}_g-\mathbf{x}_s^I|}{c_P}\right), \tag{11}$$

where $\mathbf{x}_s^I(x_s,y_s)$ denotes the position of the image source associated with the surface source at $\mathbf{x}_s = (x_s, y_s, 0)$. For our dipping reflector, the image source is found at

$$\mathbf{x}_s^I(x_s,y_s) = \mathbf{x}_s + (2z_R(x_s,y_s)\cos D)\,\mathbf{n}, \tag{12}$$

where $z_R(x_s,y_s)$ is the reflector depth below the source and

$$\mathbf{n} = -\sin D\,\mathbf{e}_1 + \cos D\,\mathbf{e}_3 \tag{13}$$

is the normal vector to the reflector. Therefore,

$$\mathbf{x}_s^I(x_s,y_s) = (x_s\cos 2D - z_d\sin 2D)\,\mathbf{e}_1 + y_s\,\mathbf{e}_2 + 2(x_s\sin D\cos D + z_d\cos^2 D)\,\mathbf{e}_3. \tag{14}$$

In a reverse time migration, the receiver wavefield is backpropagated in reverse time. In other words, an explosive source acts at the position of every geophone, where the volume injection must be equal to

$$w_b(t;\mathbf{x}_g) = p_g(\mathbf{x}_g, t_{max}-t;\mathbf{x}_s,0) = \frac{CR(\mathbf{x}_g,\mathbf{x}_s)}{|\mathbf{x}_g-\mathbf{x}_s^I|} w''\left(t_{max}-t-\frac{|\mathbf{x}_g-\mathbf{x}_s^I|}{c_P}\right). \tag{15}$$

In this way, a new source field of the form of equation (10) is generated, where the source wavelet $w(t)$ is replaced by $w_b(t)$ of equation (15). In this way, the backpropagated field within the medium is given by

$$p_b(\mathbf{x},t;\mathbf{x}_g,0) = \frac{C^2R(\mathbf{x}_g,\mathbf{x}_s)}{|\mathbf{x}-\mathbf{x}_g||\mathbf{x}_g-\mathbf{x}_s^I|}\, w''''\left(t_{max}-t+\frac{|\mathbf{x}-\mathbf{x}_g|}{c_P}-\frac{|\mathbf{x}_g-\mathbf{x}_s^I|}{c_P}\right). \tag{16}$$

Imaging condition

The imaging condition (1) for reverse time migration is given by the zero-lag cross-correlation between the forward and backward propagating wavefields (Claerbout, 1985). Considering a continuous and infinite distribution of sources and receivers over the surface, we can write

$$I(\mathbf{x}) = \int_{-\infty}^{+\infty} dx_s \int_{-\infty}^{+\infty} dy_s \int_{-\infty}^{+\infty} dx_g \int_{-\infty}^{+\infty} dy_g \int_0^{t_{max}} dt\; p_s(\mathbf{x},t;\mathbf{x}_s) p_b(\mathbf{x},t;\mathbf{x}_g)\,. \tag{17}$$

Under the assumptions of a causal source pulse and that no reflection events exist after the maximum time t_{max}, the time integral can be extended to infinity, i.e.,

$$I(\mathbf{x}) = \int_{-\infty}^{+\infty} dx_s \int_{-\infty}^{+\infty} dy_s \int_{-\infty}^{+\infty} dx_g \int_{-\infty}^{+\infty} dy_g \int_{-\infty}^{+\infty} dt\; p_s(\mathbf{x},t;\mathbf{x}_s) p_b(\mathbf{x},t;\mathbf{x}_g)\,. \tag{18}$$

Using Parseval's theorem (see, e.g., Bracewell, 1999), the time integral can now be substituted by the corresponding frequency integral, resulting in

$$I(\mathbf{x}) = \frac{1}{2\pi}\int_{-\infty}^{+\infty}\int_{-\infty}^{+\infty}\int_{-\infty}^{+\infty}\int_{-\infty}^{+\infty} dx_s dy_s dx_g dy_g \int_{-\infty}^{+\infty} d\omega\; P_s(\mathbf{x},\omega;\mathbf{x}_s) P_b^*(\mathbf{x},\omega;\mathbf{x}_g)\,, \tag{19}$$

where the asterisk denotes the complex conjugate.

Taking the Fourier transforms of the source and receiver wavefields,

$$P_s(\mathbf{x},\omega;\mathbf{x}_s) = \frac{C}{|\mathbf{x}-\mathbf{x}_s|}(-i\omega)^2 W(\omega) e^{-i\omega|\mathbf{x}-\mathbf{x}_s|/c_P} \tag{20}$$

and

$$P_g(\mathbf{x},\omega;\mathbf{x}_g) = \frac{C^2R(\mathbf{x}_g,\mathbf{x}_s)}{|\mathbf{x}-\mathbf{x}_g||\mathbf{x}_g-\mathbf{x}_s^I|}(i\omega)^4 W(\omega) e^{i\omega\left(|\mathbf{x}-\mathbf{x}_g|-|\mathbf{x}_g-\mathbf{x}_s^I|\right)/c_P} \tag{21}$$

the imaging condition integral can be expressed as

$$\begin{aligned} I(\mathbf{x}) \;=\; & \frac{C^3}{2\pi}\int_{-\infty}^{+\infty} d\omega\; (-i\omega)^6\, W^2(\omega) \\ & \left[\int_{-\infty}^{+\infty}\int_{-\infty}^{+\infty}\int_{-\infty}^{+\infty}\int_{-\infty}^{+\infty} dx_s dy_s dx_g dy_g G(\mathbf{x}_g,\mathbf{x}_s)\; e^{-i\omega\Phi(\mathbf{x}_g,\mathbf{x}_s)}\right] \end{aligned} \tag{22}$$

with

$$G(\mathbf{x}_g,\mathbf{x}_s) = \frac{R(\mathbf{x}_g,\mathbf{x}_s)}{|\mathbf{x}-\mathbf{x}_g||\mathbf{x}-\mathbf{x}_s||\mathbf{x}_g-\mathbf{x}_s^I|} \tag{23}$$

and

$$\Phi(\mathbf{x}_g,\mathbf{x}_s) = \left(|\mathbf{x}-\mathbf{x}_s|+|\mathbf{x}-\mathbf{x}_g|-|\mathbf{x}_g-\mathbf{x}_s^I|\right)/c_P\,. \tag{24}$$

Stationary phase evaluation

Following Matthew et al. (2005), the four-dimensional integral in brackets in equation (22) can be evaluated by the stationary-phase method. This methods evaluates oscillatory integrals of the type

$$I(\omega) = \int_{\Omega} G(\mathbf{x}) \exp[-i\omega\Phi(\mathbf{x})] d^n\mathbf{x} \tag{25}$$

asymptotically for large ω as (see, e.g., Bleistein and Handelson, 1975)

$$I(\omega) \approx \left(\frac{2\pi}{\omega}\right)^{n/2} \frac{G(\mathbf{x}_0)}{\sqrt{|\nabla\nabla^T\Phi(\mathbf{x}_0)|}} \exp\left[-i\omega\Phi(\mathbf{x}_0) - i\frac{\pi}{4}\mathrm{Sgn}\left(\nabla\nabla^T\Phi(\mathbf{x}_0)\right)\right] , \tag{26}$$

where $\mathbf{x}_0$ is a isolated point of stationary phase (supposed to be unique), i.e.,

$$\nabla\Phi(\mathbf{x}_0) = \mathbf{0} \tag{27}$$

and

$$|\nabla\nabla^T\Phi(\mathbf{x}_0)| \neq 0 . \tag{28}$$

Moreover, $\mathrm{Sgn}(\nabla\nabla^T\Phi(\mathbf{x}_0)$ represents the signature of the matrix, i.e., the number of positive eigenvalues minus the number of negative ones.

Stationary point.— The derivatives of the phase function (24) are

$$\frac{\partial\Phi}{\partial x_s} = \frac{1}{c_P}\left(-\frac{x-x_s}{|\mathbf{x}-\mathbf{x}_s|} + \frac{x_g\cos 2D - x_s - z_d\sin 2D}{|\mathbf{x}_g-\mathbf{x}_s^I|}\right) , \tag{29}$$

$$\frac{\partial\Phi}{\partial x_g} = \frac{1}{c_P}\left(-\frac{x-x_g}{|\mathbf{x}-\mathbf{x}_s|} - \frac{x_g - x_s\cos 2D + z_d\sin 2D}{|\mathbf{x}_g-\mathbf{x}_s^I|}\right) , \tag{30}$$

$$\frac{\partial\Phi}{\partial y_s} = \frac{1}{c_P}\left(-\frac{y-y_s}{|\mathbf{x}-\mathbf{x}_s|} + \frac{y_g-y_s}{|\mathbf{x}_g-\mathbf{x}_s^I|}\right) , \tag{31}$$

$$\frac{\partial\Phi}{\partial y_g} = \frac{1}{c_P}\left(-\frac{y-y_g}{|\mathbf{x}-\mathbf{x}_s|} - \frac{y_g-y_s}{|\mathbf{x}_g-\mathbf{x}_s^I|}\right) . \tag{32}$$

From using equations (31) and (32) in condition (27) follows that the stationary point in both the y_s and y_g integrals is at the same point y_0 defined by

$$y_0 \equiv y_s = y_g = y . \tag{33}$$

Equations (29) and (30) are symmetric in x_s and x_g. Therefore, the stationary point in both the x_s and x_g integrals is also at the same point x_0, given by

$$x_0 \equiv x_s = x_g = x + z\tan D . \tag{34}$$

Thus, at the stationary point, we have

$$G(\mathbf{x}_0,\mathbf{x}_0) = \frac{R(\mathbf{x}_0,\mathbf{x}_0)}{|\mathbf{x}-\mathbf{x}_0|^2|\mathbf{x}_0-\mathbf{x}_s^I|} \tag{35}$$

and

$$\Phi(\mathbf{x}_0,\mathbf{x}_0) = \frac{2}{c_P}\cos D\,(z - z_d + x\tan D) . \tag{36}$$

Here, $R(\mathbf{x}_0,\mathbf{x}_0)$ is the reflection coefficient for normal incidence.

Hessian matrix.— The second derivatives at the stationary point have the following nonzero components:

$$\frac{\partial^2\Phi(\mathbf{x}_0,\mathbf{x}_0)}{\partial x_s\partial x_s} = \frac{\cos^2 D}{c_P}\left(\frac{1}{|\mathbf{x}-\mathbf{x}_0|}-\frac{1}{|\mathbf{x}_0-\mathbf{x}_s^I|}\right), \tag{37}$$

$$\frac{\partial^2\Phi(\mathbf{x}_0,\mathbf{x}_0)}{\partial x_g\partial x_s} = \frac{\cos^2 D}{c_P}\left(\frac{1}{|\mathbf{x}_0-\mathbf{x}_s^I|}\right), \tag{38}$$

$$\frac{\partial^2\Phi(\mathbf{x}_0,\mathbf{x}_0)}{\partial x_g\partial x_g} = \frac{\cos^2 D}{c_P}\left(\frac{1}{|\mathbf{x}-\mathbf{x}_0|}-\frac{1}{|\mathbf{x}_0-\mathbf{x}_s^I|}\right), \tag{39}$$

$$\frac{\partial^2\Phi(\mathbf{x}_0,\mathbf{x}_0)}{\partial y_s\partial y_s} = \frac{1}{c_P}\left(\frac{1}{|\mathbf{x}-\mathbf{x}_0|}-\frac{1}{|\mathbf{x}_0-\mathbf{x}_s^I|}\right), \tag{40}$$

$$\frac{\partial^2\Phi(\mathbf{x}_0,\mathbf{x}_0)}{\partial y_g\partial y_s} = \frac{1}{c_P}\left(\frac{1}{|\mathbf{x}_0-\mathbf{x}_s^I|}\right), \tag{41}$$

$$\frac{\partial^2\Phi(\mathbf{x}_0,\mathbf{x}_0)}{\partial y_g\partial y_g} = \frac{1}{c_P}\left(\frac{1}{|\mathbf{x}-\mathbf{x}_0|}-\frac{1}{|\mathbf{x}_0-\mathbf{x}_s^I|}\right). \tag{42}$$

Therefore, the Hessian determinant is

$$\sqrt{|\nabla\nabla^T\Phi(\mathbf{x}_0)|} = \frac{2\cos^3 D}{c_P^2}\frac{|x\tan D+z_d-z|}{|\mathbf{x}-\mathbf{x}_0|^2|\mathbf{x}_0-\mathbf{x}_s^I|} \tag{43}$$

The signature of the Hessian is determined by an analysis of its eigenvalues. Because of the particular structure of the Hessian matrix, the problem reduces to the evaluation of two 2×2 submatrices,

$$\left|\begin{array}{cc}\frac{\partial^2\Phi}{\partial x_s\partial x_s}-\lambda & \frac{\partial^2\Phi}{\partial x_g\partial x_s}\\ \frac{\partial^2\Phi}{\partial x_g\partial x_s} & \frac{\partial^2\Phi}{\partial x_s\partial x_s}-\lambda\end{array}\right|_{\mathbf{x}_s=\mathbf{x}_g=\mathbf{x}_0}=0 \tag{44}$$

and

$$\left|\begin{array}{cc}\frac{\partial^2\Phi}{\partial y_s\partial y_s}-\lambda & \frac{\partial^2\Phi}{\partial y_g\partial y_s}\\ \frac{\partial^2\Phi}{\partial y_g\partial y_s} & \frac{\partial^2\Phi}{\partial y_s\partial y_s}-\lambda\end{array}\right|_{\mathbf{x}_s=\mathbf{x}_g=\mathbf{x}_0}=0\,. \tag{45}$$

This results in the eigenvalues

$$\lambda_{1,3} = \frac{1}{c_P}\frac{1}{|\mathbf{x}-\mathbf{x}_0|} = \frac{1}{c_P}\frac{\cos D}{z} \tag{46}$$

and

$$\begin{aligned}\lambda_{2,4} &= \frac{1}{c_P}\left(\frac{1}{|\mathbf{x}-\mathbf{x}_0|}-\frac{2}{|\mathbf{x}_0-\mathbf{x}_s^I|}\right)\\ &= \frac{\cos^3 D}{c_P}\,\frac{x\tan D+z_d-z}{z+(x\tan D+z_d-z)\cos^2 D}\,.\end{aligned} \tag{47}$$

Thus, eigenvalues $\lambda_{1,3}$ are always positive, while the sign of $\lambda_{2,4}$ depends on the vertical position z of the image point. We have that $\lambda_{2,4}>0$ if $z<x\tan D+z_d$, i.e., if the image point is above the reflector, and $\lambda_{2,4}<0$ below it. Therefore, the signature of the Hessian is equal to 4 for points above the reflector and 0 for points below it. Thus, the phase term in equation (26) can be represented as

$$e^{-i\frac{\pi}{4}\mathrm{Sgn}(\nabla\nabla^T\Phi(\mathbf{x}_0,\mathbf{x}_0))} = \mathrm{sgn}(z-z_d-x\tan D)\,. \tag{48}$$

Final image.— Collecting results, the image $I(\mathbf{x})$ becomes

$$I(\mathbf{x}) \approx \pi C^3 c_P^3\frac{R(\mathbf{x}_0,\mathbf{x}_0)}{\cos^3 D}\frac{\mathrm{sgn}(z-x\tan D-z_d)}{|z-x\tan D-z_d|} \tag{49}$$

$$\int_{-\infty}^{+\infty} d\omega(-i\omega)^4 W^2(\omega)e^{-i2\omega(z-z_d-x\tan D)\cos D/c_P}\,. \tag{50}$$

The frequency integral can be solved using the convolution theorem and the properties of the Fourier transform. Thus, the final representation of the image at point $\mathbf{x}$ is

$$I(\mathbf{x}) \approx \pi C^3 c_P^3 \frac{R(\mathbf{x}_0, \mathbf{x}_0)}{\cos^3 D} \frac{1}{z - z_R} w'' \left[\frac{2 \cos D}{c_P} (z - z_R) \right] \otimes w'' \left[\frac{2 \cos D}{c_P} (z - z_R) \right] , \quad (51)$$

where we have recognized that $z_d + x \tan D = z_R$ is the reflector depth at the horizontal position of the image point. As mentioned earlier, expression (51) coincides with the corresponding one of Matthew et al. (2005) except for the pulse-stretch factor, $2 \cos D / c_P$ in the arguments of both the wavelets.